

# Coherency Strain and the Kinetics of Phase Separation in LiFePO<sub>4</sub> Nanoparticles

Daniel A. Cogswell<sup>†</sup> and Martin Z. Bazant<sup>†,‡,\*</sup>

<sup>†</sup>Department of Chemical Engineering and <sup>‡</sup>Department of Mathematics, Massachusetts Institute of Technology, Cambridge, Massachusetts 02139, United States

Lithium iron phosphate (LiFePO<sub>4</sub>) has emerged as an important high-rate cathode material for rechargeable batteries<sup>1</sup> and is unique because of its strongly anisotropic diffusivity,<sup>2,3</sup> its strong elastic anisotropy,<sup>4</sup> and its tendency to phase-separate into lithium-rich and lithium-poor phases.<sup>5–9</sup>

Despite conclusive observations of phase boundaries in chemically delithiated LiFePO<sub>4</sub> nanoparticles,<sup>10–12</sup> the general consensus has been that phase boundaries always form during electrochemical discharge, thereby limiting battery performance.<sup>5,13</sup> However, this limitation is inconsistent with dramatic rate improvements resulting from smaller nanoparticles, doping,<sup>14</sup> and surface coatings.<sup>15</sup>

The feasibility of phase boundary formation has recently been challenged by both phase-field models<sup>16,17</sup> and *ab initio* calculations.<sup>18</sup> In a companion paper,<sup>17</sup> we demonstrate that high discharge currents can suppress phase separation in reaction-limited nanoparticles, making the spinodal a *dynamical* property of intercalation systems. In this paper, we consider the additional effect of elastic coherency strain and find that it leads to a quantitatively accurate phase-field description of Li<sub>x</sub>FePO<sub>4</sub> that is useful for interpreting experimental data. With mathematical analysis and numerical simulations of galvanostatic discharge, we conclude that coherency strain strongly suppresses phase separation, leading to better battery performance and improved mechanical durability.

Coherency strain arises when molar volume is a function of composition, that is, due to the difference in lattice parameters between FePO<sub>4</sub> and LiFePO<sub>4</sub>. Two-phase systems with identical crystal structure and small misfit strains generally form coherent interfaces.<sup>19,20</sup> It has been suggested that Li<sub>x</sub>FePO<sub>4</sub> retains coherency throughout nucleation and growth,<sup>9</sup> and *in situ* observation of crystalline

## ABSTRACT



A theoretical investigation of the effects of elastic coherency strain on the thermodynamics, kinetics, and morphology of intercalation in single LiFePO<sub>4</sub> nanoparticles yields new insights into this important battery material. Anisotropic elastic stiffness and misfit strains lead to the unexpected prediction that low-energy phase boundaries occur along {101} planes, while conflicting reports of phase boundary orientations are resolved by a partial loss of coherency in the [001] direction. Elastic relaxation near surfaces leads to the formation of a striped morphology with a characteristic length scale predicted by the model, yielding an estimate of the interfacial energy. The effects of coherency strain on solubility and galvanostatic discharge are studied with a reaction-limited phase-field model that quantitatively captures the influence of misfit strain, particle size, and temperature on solubility seen in experiments. Coherency strain strongly suppresses phase separation during discharge, which enhances rate capability and extends cycle life. The effects of elevated temperature and the feasibility of nucleation are considered in the context of multiparticle cathodes.

**KEYWORDS:** Li-ion battery · LiFePO<sub>4</sub> · phase-field model · coherency strain · phase boundaries · stripe morphology · Butler–Volmer kinetics

material during battery operation supports this prediction.<sup>21,22</sup>

As we show, the observation of aligned phase boundaries and striped morphologies in Li<sub>x</sub>FePO<sub>4</sub><sup>10–12</sup> provides conclusive evidence of coherency strain. Furthermore, it is necessary to consider the fully anisotropic elastic constants and misfit strain to interpret experiments. Simplified elastic analysis has led to the conclusion that {100} is always the preferred orientation,<sup>23,24</sup> although {101} phase boundaries are sometimes observed.<sup>11,12</sup> Our fully anisotropic analysis predicts that {101} is the low-energy orientation, and we attribute the observation of {100} boundaries to a partial loss of coherency resulting from dislocations (or cracks).

\* Address correspondence to bazant@mit.edu.

Received for review October 30, 2011 and accepted February 3, 2012.

Published online  
10.1021/nn204177u

© XXXX American Chemical Society

The origin of striped morphologies<sup>10</sup> has not been satisfactorily explained. It has been suggested that they result from the characteristic wavelength of spinodal decomposition,<sup>12</sup> although it is not clear why the instability would be frozen in this state. We show instead that stripes represent the stable equilibrium state of finite size particles and predict that the spacing scales with the square root of particle size. As a result, we are able to extract the interfacial energy from experimental micrographs.

The reported solubility of Li in FePO<sub>4</sub> varies significantly and depends on particle size and temperature.<sup>8–10,21,23,25–28</sup> These differences in solubility can now be explained in light of coherency strain. Phase-field calculations of solubility as a function of particle size and temperature are able to fit experimental data with just two parameters.

An alternative to coherent phase separation is for entire particles to remain homogeneous and form a mosaic, with some particles existing at low concentration and others at high concentration.<sup>21,29,30</sup> This scenario is energetically favorable since there is no phase boundary energy or change in solubility, but it requires exchange of material between nanoparticles. By constructing phase diagrams for both the coherent and mosaic scenarios, we find a limited role for coherent nucleation and growth and predict that moderately elevated temperatures ought to suppress all two-phase coexistence, even in large particles.

**Phase-Field Model.** We begin with the reaction-limited phase-field model for ion intercalation in single nanoparticles from our prior work<sup>17,31,32</sup> and extend it to include coherency strain. The theory couples electrochemical surface reactions to bulk phase separation using a thermodynamically consistent generalization of Butler–Volmer kinetics. The reaction rate depends on the Cahn–Hilliard<sup>33</sup> (or van der Waals)<sup>34</sup> gradient energy, introduced to model the formation of phase boundaries.

Individual nanoparticles are modeled as open thermodynamic systems in contact with an electrolyte mass reservoir at constant temperature, pressure, and chemical potential. To incorporate phase boundaries, we begin with the free energy functional of Cahn and Hilliard that includes coherency strain<sup>19,20,33</sup> and introduce constraints to account for constant pressure<sup>35</sup> and constant potential<sup>36</sup> which are imposed on the particle. The resulting Gibbs free energy functional is

$$G[c(\vec{x}), \vec{u}(\vec{x})] = \int_V \left\{ \rho_s [f(c) + e\Delta\phi c] + \frac{1}{2} \kappa (\nabla c)^2 + \frac{1}{2} C_{ijkl} \epsilon_{ij} \epsilon_{kl} - \bar{\sigma}_{ij} \bar{\epsilon}_{ij} \right\} dV \quad (1)$$

where  $c(\vec{x})$  is the mole fraction of lithium,  $\vec{u}(\vec{x})$  is a displacement vector,  $\rho_s$  is the number of lithium sites per unit volume,  $f(c)$  is the homogeneous Helmholtz

free energy per lithium site,  $\Delta\phi$  is the interfacial voltage at the particle surface,  $\kappa$  is the gradient energy coefficient that introduces interfacial energy,  $(1/2)C_{ijkl}\epsilon_{ij}\epsilon_{kl}$  is elastic strain energy,  $C_{ijkl}$  is the elastic stiffness tensor,  $\bar{\sigma}_{ij}$  is an applied external stress tensor, and  $\bar{\epsilon}_{ij}$  is the homogeneous component of elastic strain. Here,  $\sigma_{ij} = C_{ijkl}\epsilon_k(\vec{x})$  is the stress field, and  $\epsilon_{ij}(\vec{x})$  is the elastic strain field

$$\epsilon_{ij}(\vec{x}) = \bar{\epsilon}_{ij} + \frac{1}{2}(u_{i,j} + u_{j,i}) - \epsilon_{ij}^0 c(\vec{x}) \quad (2)$$

with three contributions,<sup>37</sup> respectively: homogeneous strain  $\bar{\epsilon}_{ij}$ , strain resulting from compositional inhomogeneity, and stress-free inelastic strain assumed to vary linearly with composition (Vegard's Law), where  $\epsilon_{ij}^0$  is the lattice misfit between FePO<sub>4</sub> and LiFePO<sub>4</sub>.

Physically,  $\bar{\epsilon}_{ij}$  is the homogeneous component of total strain that is applied everywhere to reach equilibrium with the external pressure.<sup>35</sup> It minimizes eq 1 when the system is in mechanical equilibrium with an applied stress state  $\bar{\sigma}_{ij}$ . Treating strain in this way assumes that  $\epsilon_{ij}^0 c(\vec{x})$  is heterogeneous on the microscopic scale but homogenous on the macroscopic scale of the particle; that is, the macroscopic system is significantly larger than the length over which the misfit strain changes (the interfacial width). Particles bathed in electrolyte are in a state of hydrostatic stress so that  $\bar{\sigma}_{ij} = -P\delta_{ij}$ , where  $P$  is the pressure in the electrolyte, and  $\delta_{ij}$  is a Kronecker delta. For solids, "PV work" is generally very small and can be neglected at atmospheric pressure, and thus in eq 1 we consider free expansion of the particle at  $P = 0$ .

Since elastic relaxation is much faster than diffusion, the displacement vector  $\vec{u}(\vec{x})$  is determined from mechanical equilibrium ( $\delta G/\delta \vec{u} = 0$ ):

$$\nabla \cdot \sigma_{ij} = 0 \quad (3)$$

Following Garcia *et al.*, who introduced a Lagrange multiplier for the electrochemical potential,<sup>36</sup> we also define  $\Delta\phi$  in eq 1 as a Lagrange multiplier for a constraint on the composition field such that  $\int_V c(\vec{x}) dV = X$ , where  $X$  is the mean state of charge (i.e., Li<sub>x</sub>FePO<sub>4</sub>). In order to connect thermodynamics with electrochemistry,<sup>17,38,39</sup> we identify  $\Delta\phi = \phi - \phi_e$  as the interfacial voltage of the Faradaic half-cell reaction, Li  $\leftrightarrow$  Li<sup>+</sup> + e<sup>-</sup>, where  $\phi$  and  $\phi_e$  are the electrostatic potentials of ions and electrons, respectively. In equilibrium, there is a unique potential difference, the Nernst voltage  $\Delta\phi_{eq}$ , which minimizes eq 1 once the state of charge has been defined. When a potential  $\Delta\phi \neq \Delta\phi_{eq}$  is applied, the system is displaced from equilibrium, and lithium enters or leaves the system until  $\Delta\phi = \Delta\phi_{eq}$ , at which point the constraint on the composition field is obeyed and equilibrium is reached.

It is now possible to define the overpotential  $\eta$  in a variational sense for phase-separating intercalation

systems:

$$\eta(c, \nabla^2 c, \vec{u}) = \Delta\phi - \Delta\phi_{\text{eq}} = \frac{1}{e\mu_s} \frac{\delta G}{\delta c} \quad (4)$$

Since  $\eta = 0$  at equilibrium, we see that  $\eta$  is the driving force for intercalation in systems that are out of equilibrium and is equivalent to the variational derivative of the energy functional (eq 1). It is a subtle but important point that we define overpotential relative to the Nernst voltage rather than the voltage plateau of the phase-separated system at zero current. The Nernst voltage is an equilibrium material property, but the voltage plateau is an emergent property of the entire cathode. A flat voltage plateau is commonly cited as a hallmark of phase separation, but as we will demonstrate, coherency strain leads to upward-sloping plateaus in single particles.

With these definitions, a thermodynamically consistent theory of the Faradaic (charge transfer) current density  $J$  at the surface of the particle can be derived, based on a generalized Butler–Volmer equation for solids and concentrated solutions:<sup>17,38,39</sup>

$$J = J_0 [e^{-\alpha e\eta/kT} - e^{(1-\alpha)e\eta/kT}],$$

$$J_0 = k_0 \frac{a_+^{1-\alpha} a^\alpha}{\gamma_A}, \quad \Delta\phi_{\text{eq}} = \frac{kT}{e} \ln \frac{a_+}{a} \quad (5)$$

where  $J_0$  is the exchange current density,  $a_+$  is the lithium ion activity in the electrolyte, and  $a$  is the intercalated lithium activity. The activities are related to  $\Delta\phi_{\text{eq}}$  by the Nernst equation. Following Bai *et al.*,<sup>17</sup> we set the activity coefficient of the activated state,  $\gamma_A = (1 - c)^{-1}$ , to account for site exclusion,  $a_+ = 1$  to neglect electrolyte concentration variations, and  $\alpha = 1/2$  for symmetric charge transfer. It is crucial that the reaction rate depends not only on the lithium concentration,  $c$ , but also on its Laplacian,  $\nabla^2 c$  (*via* the Cahn–Hilliard gradient energy) and on the elastic displacement  $\vec{u}$  (*via* coherency strain energy). As predicted by Singh *et al.*,<sup>31</sup> the reaction rate is thus amplified at phase boundaries, causing them to propagate like waves at sufficiently low current.<sup>17</sup> Here, we show how these phenomena are affected by coherency strain.

To model the experimentally relevant case of galvanostatic discharge, the current flow into the particle is constrained by an integral over the active area at the surface of the particle:

$$I = \int_A \frac{\partial c}{\partial t} dA,$$

$$\frac{\partial c}{\partial t} = J_0 [e^{-\alpha e\eta/kT} - e^{(1-\alpha)e\eta/kT}] + \xi \quad (6)$$

where  $\xi$  is a Langevin noise term. These equations are the boundary conditions for intercalation at the particle surface. To account for the bulk of the particle, we use a depth-averaged approximation<sup>17,31,32</sup> where

eq 6 constitutes a 2D system of equations that can be solved on the particle's active surface for the mean concentration  $c$  in each lithium channel. This approximation is valid for sufficiently small nanoparticles (<100 nm, mostly free of Li/Fe antisite defects),<sup>40,41</sup> where diffusion in channels along the  $b$ -axis is much faster than surface reactions, leading to a quasi-steady concentration profile in the depth direction. As we show below, anisotropic elasticity favors homogeneity in the  $b$  direction (Figure 1), a prediction supported by phase-field simulations of diffusion in the lithium channels.<sup>42</sup>

Finally, the elastic model is reduced to 2D by assuming plane strain and neglecting displacements in the  $b$  direction. This is reasonable since the lithium channels are much longer than their (atomic scale) thickness. The simulations below further assume finite square particles with stress-free boundaries. We use a natural boundary condition,  $\hat{n} \cdot \nabla c = 0$ , which assumes that the surface energy does not change with state of charge and imposes a contact angle between the phase boundary and the particle surface of 90°. More numerical details can be found in the Methods section.

## RESULTS

**Phase Boundary Orientation.** Since LiFePO<sub>4</sub> is orthorhombic, it is necessary to consider its fully anisotropic elastic stiffness and lattice mismatch when analyzing phase boundary morphology. Assuming that the elastic modulus of each phase is the same (homogeneous modulus assumption), Khachaturyan<sup>37,43</sup> related the elastic energy of an arbitrarily anisotropic elastic inclusion to a function of direction:

$$B(\vec{n}) = C_{ijkl} \epsilon_{ij}^0 \epsilon_{kl}^0 - \vec{n}_i \sigma_{ij}^0 \Omega_{jl}(\vec{n}) \sigma_{lm}^0 \vec{n}_m \quad (7)$$

$\vec{n}$  is the interface normal, and  $\Omega$ , which is related to the elastic Green's tensor, is defined by its inverse tensor  $\Omega_{ij}^{-1} = C_{iklj} \vec{n}_k \vec{n}_l$ . Elastic energy is a function of orientation  $\vec{n}$  because a phase boundary produces zero strain in the normal direction. The direction  $\vec{n}_0$  that minimizes eq 7 defines the habit plane, which is the elastically preferred orientation of the phase boundary that minimizes strain energy.

Equation 7 is plotted in Figure 1a for FePO<sub>4</sub> using anisotropic elastic constants calculated *via* first-principles<sup>4</sup> and experimentally measured anisotropic lattice mismatch.<sup>10</sup> The figure reveals that {010} and {001} interfaces are high-energy, which justifies *a posteriori* the depth-averaged approximation which assumes fast diffusion and no phase separation in the {010} depth direction. The orientation of  $\vec{n}_0$  was obtained by numerical minimization and is drawn in red. There are four minima which lie along the {101} family of crystal planes, and  $B(\vec{n}_0) = .19$  GPa.

Figure 2a,c compares the simulated {101} phase boundaries with experimental observations by

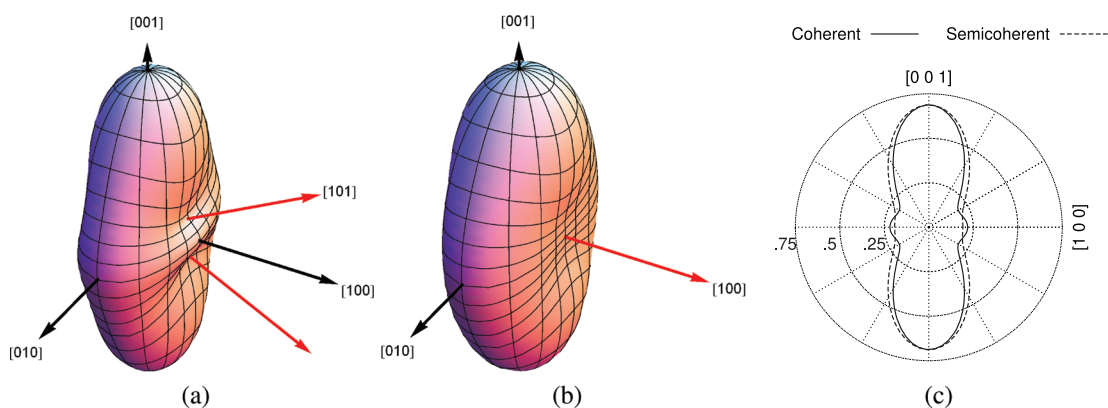


**Figure 1.** Spherical plots of  $B(\vec{n})$ , the elastic strain energy of a flat interface as a function of normal direction for (a) a coherent interface and (b) a semicoherent interface which has lost coherency in the [001] direction. The red arrows indicate  $\vec{n}_0$ , the direction of minimum energy. (c) Polar plot of  $B(\vec{n})$  in the  $a-c$  plane comparing coherent and semicoherent energies. Energy is in units of GPa.

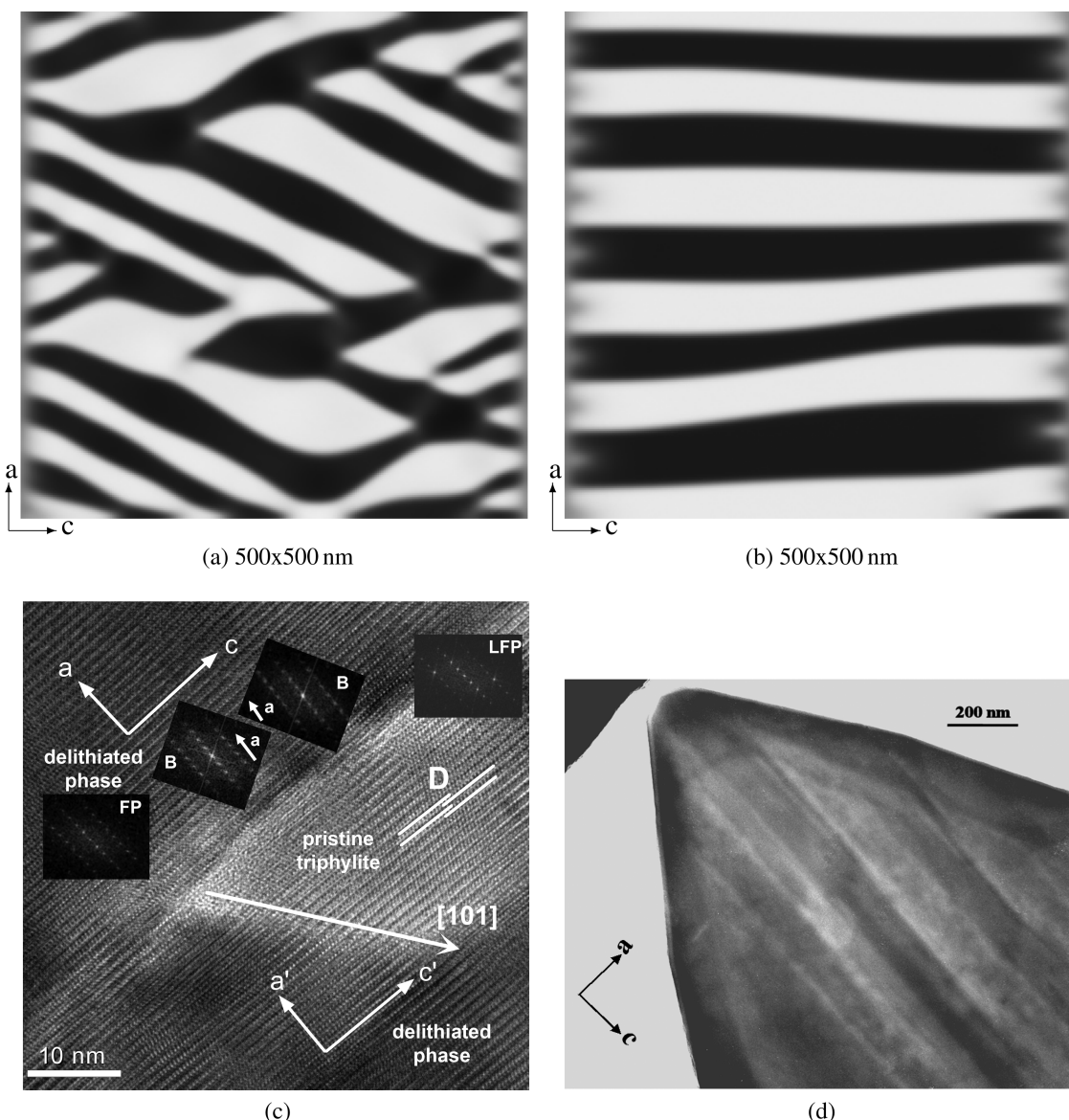


**Figure 2.** Comparison of simulated and experimental  $\text{Li}_{0.5}\text{FePO}_4$  microstructures. See Figure 3 for simulation dynamics. (a) Phase boundaries align along  $\{101\}$  planes to minimize elastic coherency strain. (b) Loss of coherency in the [001] direction causes the stripes to form along  $\{100\}$  planes. (c) HRTEM image of a  $\{101\}$  phase boundary. Reprinted from ref 12 with permission from Elsevier. (d) TEM image of  $\{100\}$  stripes.<sup>10</sup> Reproduced by permission of The Electrochemical Society.

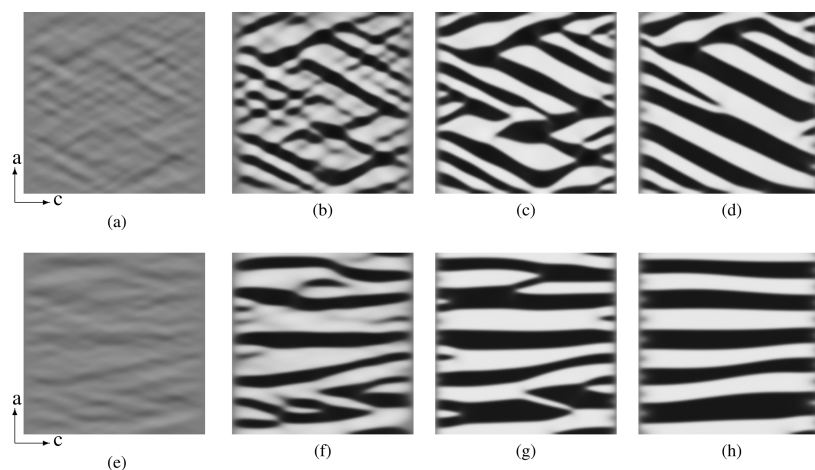


**Figure 3.** Initially homogeneous system ( $\text{Li}_{0.5}\text{FePO}_4$ ,  $500 \times 500 \text{ nm}$ ) decomposes into regions of high and low lithium concentration when held at zero current. (a–d) Phase boundaries align along  $\{101\}$  planes to minimize elastic coherency strain. (e–h) Loss of coherency in the  $[001]$  direction results produces  $\{100\}$  interfaces. See Supporting Information for movies.

Ramana *et al.*<sup>12</sup> Laffont *et al.* also appear to have observed a  $\{101\}$  interface in Figure 2b of ref 11.

However,  $\{100\}$  interfaces have been reported in some experiments,<sup>10,12</sup> even though according to Figure 1a this orientation should not be elastically preferred. The resolution to this apparent discrepancy may be the formation of dislocations that lead to a loss of coherency in  $[001]$ , the direction of *negative* misfit strain. Indeed, Chen *et al.*<sup>10</sup> report observing cracks and dislocations running along phase boundaries in the  $[001]$  direction.

Stanton and Bazant<sup>44</sup> recognized the importance of negative misfit for  $\text{LiFePO}_4$  with isotropic elastic analysis, but here we consider the fully anisotropic case. Figure 1b plots  $B(\vec{n})$  for a semicoherent interface with  $\varepsilon_{33}^0 = 0$ , and Figure 1c compares the coherent and semicoherent cases in cross section. The semicoherent habit plane lies along the  $\{100\}$  family of planes, and curiously  $B(\vec{n}_0)$  remains unchanged by the loss of coherency. The orientation of the interface changes, but its elastic energy does not. Simulation and experimental observation of  $\{001\}$  interfaces are compared in Figure 2b,d.

The mechanism by which coherency is lost remains to be determined. It could be that the phases initially form coherently but then lose coherency over time as dislocations form. It is also possible that phase boundaries form semicoherently upon lithiation, aligned with pre-existing cracks or defects.

**Equilibrium Morphology.** Modulated structures resulting from coherency strain are often observed in experimental systems, and stripes are an equilibrium morphology that minimizes energy in finite size particles.<sup>37,45</sup> Stripes form due to elastic relaxation at the surface of the particle and align normal to  $\vec{n}_0$ . The characteristic wavelength  $\lambda$  of the stripes balances the elastic energy of surface relaxation which scales with volume, and total interfacial energy which scales with

particle size.<sup>37,45</sup> Evidence of this relaxation is visible near the boundaries of the simulated particle in Figure 2b.

The wavelength of periodicity is described by a scaling relation derived in the Methods section:

$$\lambda = \sqrt{\frac{2\gamma L_c}{\Delta f}} \quad (8)$$

where  $\lambda$  is the period of the striping,  $\gamma$  is interfacial energy,  $L_c$  is the width of the particle in the  $[001]$  direction, and  $\Delta f$  is the difference in free energy density between the homogeneous state and the coherent phase-separated state;  $\Delta f$  has a chemical contribution from the homogeneous free energy density  $f(c)$  and an elastic contribution from coherency strain (eq 9). We estimate  $\Delta f = 4.77 \text{ MJ/m}^3$  using the regular solution model and gradient energy that were fitted to experimental data in Methods.

Phase-field simulation and experimental observation of stripes are compared in Figure 2b,d. Using eq 8, the striping in Figure 2d can be used to obtain the  $\text{FePO}_4/\text{LiFePO}_4$  interfacial energy. Applying eq 8 to the striped pattern in Figure 2d, with  $L_c = 4 \mu\text{m}$  and  $\lambda \approx 250 \text{ nm}$  (measured away from the corner to mitigate the influence of particle geometry), we infer a phase boundary energy of  $37 \text{ mJ/m}^2$ . For the phase-field simulation in Figure 2d,  $L_c = 500 \text{ nm}$ ,  $\lambda \approx 90 \text{ nm}$ , and  $\gamma = 39 \text{ mJ/m}^2$  according to eq 8. The interfacial energy can also be calculated directly from the phase-field model,<sup>33,46</sup> which yields  $\gamma = 39 \text{ mJ/m}^2$ . This value of  $\gamma$  follows the rule of thumb that coherent interfaces have interfacial energies less than  $200 \text{ mJ/m}^2$ ,<sup>47</sup> and it confirms both the validity of the scaling relation and our choice of phase-field parameters (in particular  $\kappa$ , which has until now been difficult to estimate).

Figure 3 shows the dynamics of phase separation for a homogeneous particle of composition  $\text{Li}_{0.5}\text{FePO}_4$

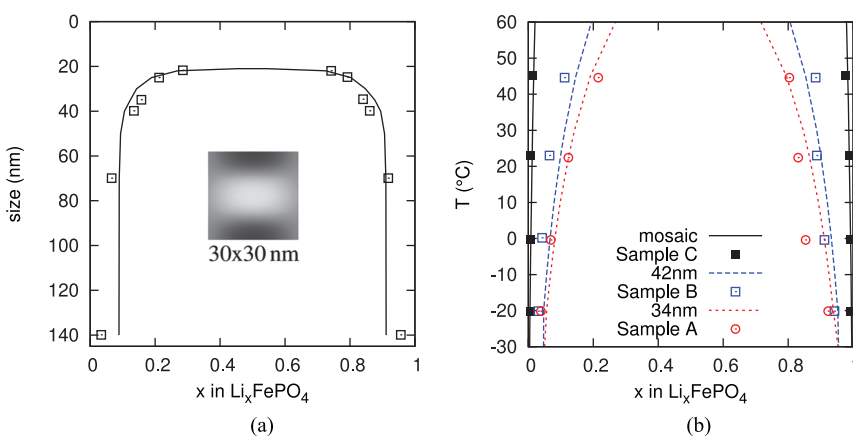


**Figure 4.** Comparison of calculated and measured  $\text{LiFePO}_4$  solubility limits as a function of temperature and particle size. (a) Size dependence at room temperature. Data points from ref 28. (b) Size and temperature dependence. Data points from ref 9.

that is held at zero current. This might correspond to a particle which is allowed to relax after having been rapidly discharged to  $x = 0.5$  (so that it remains homogeneous). Both the coherent and semicoherent cases are shown. The initial decomposition is followed by a period of coarsening, but coarsening stops when the stripes reach their characteristic wavelength, which scales with  $\sqrt{L_c}$ . Thus the stripes are dependent on particle geometry and do not coarsen, as would be expected if they were related to the most unstable wavelength of spinodal decomposition.<sup>12</sup>

**Critical Particle Size.** Phase-field methods have been used in studies of size-dependent solubility without coherency strain,<sup>39,48</sup> and a minimum system size was found below which two-phase coexistence is prohibited. This minimum size is set by the diffuse width of the phase boundary. Here we find that the critical particle size criterion changes with the introduction of coherency strain.

Figure 4 compares phase-field calculations and measurements of the solubility limits as a function of particle size and temperature. A regular solution was used for  $f(c)$ , and the regular solution parameter  $\Omega$  and gradient energy  $\kappa$  were obtained with a least-squares regression of the phase-field model to the data points in Figure 4 (see Methods). With just these two parameters, we were able to simultaneously fit both size and temperature dependence of lithium solubility (four experimental data sets). This confirms that the  $\text{Li}_x\text{FePO}_4$  system may reasonably be described as a regular solution.

The fitting in Figure 4b offers new insight into the experiments themselves. In ref 9, the differences in the miscibility gap were originally thought to be related to particle size, but according to Figure 4, 100 nm and 42 nm particles should not show significantly different solubilities. As Figure 4b shows, the shrinking miscibility gap in samples A and B is plausibly explained by coherency strain. This assertion is confirmed by X-ray diffraction (XRD) analysis in the paper, which found strain

in samples A and B but not in C. Samples A and B were prepared differently than C, which may explain why phase boundaries did not form in sample C.

The equilibrium phase boundary width was measured from simulation to be 12 nm, which is in good agreement with the 12–15 nm width measured by STEM/EELS.<sup>11</sup> In phase-field simulations of small particles near the critical size, we observed that phase separation always occurs as a sandwich (see Figure 4a inset), sometimes with the lithiated phase in the middle, and other times with the delithiated phase in the middle. Presumably, this is a result of elastic interaction between the phases. Both cases require the formation of two interfaces, explaining why the critical particle size of 22 nm is roughly twice the interfacial thickness.

**Phase Diagram.** Figure 5 shows a phase diagram that was calculated using the fitted regular solution model (see Methods). The mosaic phase diagram was calculated using  $f(c)$ , and the coherent phase diagram was calculated by adding elastic energy via eq 9 to  $f(c)$ . The eutectoid reaction<sup>6,7</sup> involving a disordered phase at higher temperatures has been neglected. The phase diagram reveals that coherency strain stabilizes the solid solution at temperatures above 150 °C, well below the disordering temperature.

The illustrations in Figure 5 depict nanoparticles in a completely delithiated cathode that has been discharged to the corresponding points in the phase diagram. At point A, the particles are inside the mosaic miscibility gap but do not transform since there is no phase transformation pathway. The microstructure is thus metastable with respect to mosaic decomposition. At point B, the particles cross the coherent miscibility and coherent nucleation inside particles becomes possible. Phase transformation will proceed slowly in this region since nucleation is an activated process, and for fast discharge, this region will be bypassed.

By point C, the particles have crossed the mosaic spinodal and spontaneously form a mosaic if they are able to exchange ions through the electrolyte. Current

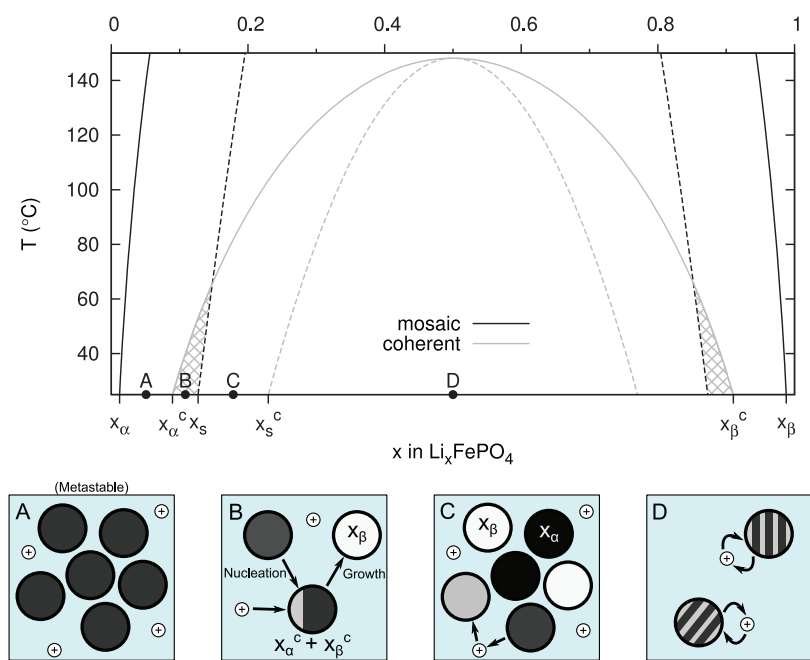


**Figure 5.** Phase diagram comparing coherent and mosaic phase separation. Solid lines are the limits of miscibility, and dashed lines indicate the spinodal. Hashing denotes the region where coherent nucleation is feasible. The illustrations depict a fully delithiated cathode that has been discharged to points A, B, C, and D in the phase diagram. Particles exchange lithium in A, B, and C. In D, discharge occurs rapidly to a point inside the coherent spinodal without time for exchange of ions between particles. The particles only exchange lithium with their immediate surroundings.

plays an important role in the onset of this transition since the position of the spinodal moves inward and eventually disappears with increasing current,<sup>17</sup> as we calculate in the next section.

Point D illustrates the case where particles exchange lithium with their immediate surroundings but do not freely exchange lithium with each other. Discharge occurs rapidly to a point inside the coherent spinodal without time for exchange of ions between particles, and the particles relax to a phase-separated state. This case might result from chemical delithiation,<sup>8,10,12,26,28</sup> a high degree of Li antisite defects,<sup>27</sup> the particle size and spacing, or even the synthesis technique itself.<sup>9,23</sup> All of these appear to influence the formation of phase boundaries.

The difference in solubilities predicted in Figure 5 can be used as a guide to the interpretation of experimental data. If a mosaic forms, the existence of a second phase first becomes possible inside the mosaic solubility limits, and particles will have compositions of either  $x_\alpha = 0.01$  or  $x_\beta = 0.99$ . XRD measurements of a system of fully intercalated and fully deintercalated individual particles confirms the appearance of a second phase by  $x = 0.04$  at room temperature,<sup>21</sup> and equilibrium measurements find very little room temperature solubility.<sup>9,25</sup>

However, if coherent phase boundaries form inside particles, the onset of phase separation in Figure 5 will only occur for  $0.09 < x < 0.91$ . Frequent reports of extended regions of solid solution<sup>8–10,23,26–28</sup> support this prediction, and several authors<sup>23,26</sup> have attributed

their observations to retained strain. Moreover, the XRD measurements of Chen *et al.*<sup>10</sup> on striped particles did not detect phase separation until at least 10% of the lithium had been extracted. Badi *et al.*<sup>27</sup> also recently measured the composition of coexisting  $\text{Li}_\alpha\text{FePO}_4$  and  $\text{Li}_\beta\text{FePO}_4$  phases and found  $\alpha \approx 0.1$  and  $\beta \approx 0.9$ . Both of these observations agree precisely with the predicted coherent miscibility gap in Figure 5 at room temperature.

**Phase Separation at Constant Current.** Spinodal decomposition in systems with coherency strain was studied by Cahn,<sup>19,20</sup> who found that for homogeneous systems at equilibrium, strain energy can be approximated for small fluctuations as

$$\frac{1}{2} C_{ijkl} \varepsilon_{ij} \varepsilon_{kl} \approx \frac{1}{2} B(\bar{n}_0)(c - X)^2 \quad (9)$$

Since strain energy is a function of the mean composition of the system, coherency strain invalidates the common tangent construction and leads to an upward-sloping voltage plateau.<sup>24</sup>

A linear stability analysis of the evolution equations (eq 6) at constant current was performed by Bai *et al.*,<sup>17</sup> and the amplification factor was found to be

$$s = -\sqrt{\bar{J}_0 + \frac{l^2}{4}} (\bar{\eta}' + \kappa k^2) + l \left( \frac{\bar{J}_0}{J_0} + \frac{1}{2} \kappa k^2 \right) \quad (10)$$

Bar notation indicates evaluation of functions at the homogeneous state  $c = X$ . The overpotential  $\eta$  is approximated for small perturbations by inserting

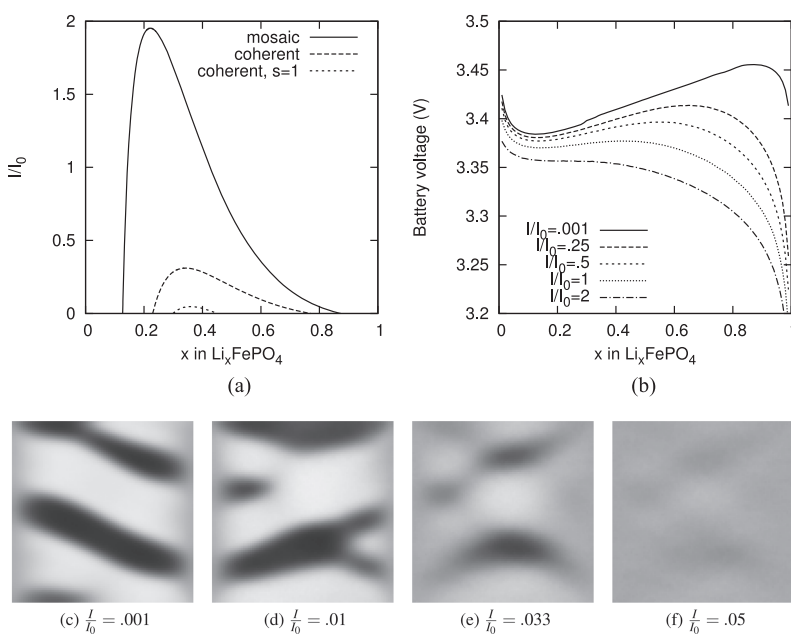


**Figure 6.** Analysis and simulation of galvanostatic discharge. (a) Linear stability boundary as a function of current. (b) Constant-current discharge curves for a single nanoparticle with coherent interfaces. (c–f) Phase boundary morphology showing formation of a quasi-solid solution as discharge rate is increased ( $\text{Li}_{0.6}\text{FePO}_4$ ,  $100 \times 100 \text{ nm}$ ). See Supporting Information for movies.

eq 9 into eq 1 and taking the variational derivative:

$$\eta = f'(c) - \kappa \nabla^2 c + B(\vec{n}_0)(c - X) \quad (11)$$

Linear stability with and without coherency strain is presented in Figure 6a. The curves show a transition from phase separating to homogeneous filling as current increases. Coherency strain promotes the stability of the solid solution by reducing the critical current and shrinking the spinodal. The neutral stability curves in the figure represent the boundary between stable and unstable dynamics ( $s = 0$ ), and the  $s = 1$  curve is where the amplification factor is large enough to produce phase separation on the order of the discharge time. This curve is an indicator of when complete phase separation is observable and has a maximum at  $I/I_0 = 0.047$ , where  $I$  is the applied current and  $I_0$  is the exchange current. In between the coherent curve and the  $s = 1$  curve is a region of *quasi-solid solution* where there are unstable modes, but not enough time for complete phase separation.<sup>17</sup>

The transition from fully phase separating to quasi-solid solution is captured in the simulated microstructures of Figure 6, which show  $\text{Li}_{0.6}\text{FePO}_4$  at different currents. By  $I/I_0 = 0.05$  (slightly above the maximum of the  $s = 1$  curve), phase separation is just barely visible. Thus we conclude that, due to coherency strain, phase separation is suppressed when the applied current exceeds only a few percent of the exchange current.

Voltage curves during discharge were calculated at different currents and are presented in Figure 6d. The most striking difference compared to the incoherent case<sup>17</sup> is the upward-sloping voltage plateau when

phase separation occurs, which was predicted at equilibrium by Van der Ven *et al.*<sup>24</sup> The first ions to enter the particle do extra mechanical work straining the surrounding lattice, and this work is recovered by the last ions, which enter lattice sites that have already been partially strained. When phase separation is suppressed at higher currents, however, there are no phase boundaries and hence coherency strain does not play any role.

## DISCUSSION

According to Figure 5, temperature may play an important role in improving battery performance. Most battery research focuses on room temperature operation where discharge passes through the hatched region of Figure 5. Nucleation is possible in this region since the coherent miscibility is crossed before the mosaic spinodal. However, for temperatures greater than 70 °C, the situation reverses, and the mosaic instability occurs before coherent nucleation. Therefore, moderately elevated temperatures could be useful for stabilizing the solid solution. Homogeneous particles have advantages for battery performance since they have larger active area for insertion and do not waste energy forming phase boundaries. They also avoid the internal stresses caused by phase boundaries, which benefits cycle life. Furthermore, elevated temperature leads to improved kinetics. Indeed, Andersson *et al.*<sup>49</sup> observed a large increase in capacity when cycling  $\text{LiFePO}_4$  at 60 °C compared to room temperature.

$\text{LiFePO}_4$  appears to be limited by the stability of the electrolyte rather than the material itself. With

appropriately chosen electrolytes that are stable at high temperatures, LiFePO<sub>4</sub> cells have shown good thermal stability and improved capacity at temperatures up to 150 °C,<sup>50</sup> with cells even having been cycled at 250 °C.<sup>51</sup> It is important to note that this temperature effect could impact accelerated aging tests, which are performed at high temperatures and then extrapolated to room temperature using empirical models.

The fact that we calculate a small phase boundary energy  $\gamma$  may have significant consequences for the role of nucleation at small currents. Cahn and Hilliard showed that nucleation and growth competes with spinodal decomposition near the limit of metastability.<sup>20,52</sup> In the case of Figure 5, the energy barrier for nucleation in the hashed region is important. Applying the approximation of Cahn and Hilliard, we estimate the room temperature energy of coherent homogeneous nucleation to be 102 kT at the mosaic spinodal. Although this energy is fairly large, heterogeneous nucleation at the particle surface is a more likely pathway in small nanoparticles with a large surface to volume ratio. The heterogeneous nucleation barrier is likely to be only a fraction of the homogeneous barrier, placing heterogeneous nucleation well within the realm of kinetic relevance. Energy barriers must generally be less than 78 kT for observable rates of nucleation.<sup>47</sup>

The change in surface energies of the particles during lithiation may also be important. The difference in surface energy between lithiated and delithiated iron phosphate is much larger than  $\gamma$ ,<sup>53</sup> and so the lithiated phase will likely wet some facets of the external particle surface, further reducing the overpotential required for nucleation.<sup>17</sup> Therefore, our future work will focus on accurately calculating the critical nucleus and heterogeneous nucleation barrier energy in order to understand the role of nucleation.

## CONCLUSION

In this paper, we have presented a thermodynamically consistent phase-field model for nanoparticulate intercalation materials and focused on the significance of coherency strain in the Li<sub>x</sub>FePO<sub>4</sub> two-phase system. With just two free parameters (the regular solution parameter  $\Omega$  and the gradient energy  $\kappa$ ), our model simultaneously explains observed phase boundary

orientations, stripe morphologies, the measured phase boundary width, interfacial energy, size and temperature-dependent solubilities, and reports of extended solid solution.

Elastic analysis reveals that {101} is the preferred phase boundary, that negative misfit strain along the [001] axis explains the observation of {100} phase boundaries, and that elastic relaxation at the surface of the particles is the origin of stripes. Analysis and simulation of galvanostatic discharge shows that coherency strain significantly suppresses phase separation during discharge and leads to upward-sloping voltage curves for single particles below the critical current. By deriving a simple scaling relation, we have been able to estimate the phase boundary energy by measuring the stripe wavelength in an experimental micrograph. Our formula predicts  $\gamma = 39$  mJ, in precise agreement with the calculated value from the phase-field model. This small interfacial energy suggests that nucleation may play a limited role in the phase transformation process.

Using the single particle description (neglecting macroscopic gradients in porous electrodes), the behavior of a cathode composed of a large number of nanoparticles was also considered. Whereas a state of phase separation is the equilibrium state for a single particle held at zero current, a mosaic pattern is the equilibrium state for a collection of particles that can exchange lithium. This results in a phase diagram for the mosaic system which is different from the coherent phase diagram, leading to the prediction that elevated temperatures, which favor the mosaic mechanism, may be beneficial for battery performance.

In conclusion, although phase boundaries have been observed experimentally, we suspect that most electrochemical data for high rate LiFePO<sub>4</sub> are inconsistent with phase boundaries forming inside nanoparticles. This is largely a dynamical effect since our theory predicts that coherency strain reduces the critical current for homogeneous intercalation to only a few percent of the exchange current. This very strong suppression of phase separation during battery operation helps to explain why LiFePO<sub>4</sub> nanoparticles have much greater rate capability and cycle life than the original material.<sup>5</sup>

## METHODS

**Numerical Methods.** Equation 6 and Equation 3 were solved in 2D as a coupled system of differential algebraic equations using finite difference methods on a square grid. Dirichlet boundary conditions,  $\bar{u} = 0$ , were applied to displacements, and Neumann boundaries,  $(\partial c / \partial \bar{n}) = 0$ , were applied to concentration. This boundary condition on  $c$  imposes a contact angle between the phase boundary and the surface of 90° and assumes that the surface energies of FePO<sub>4</sub> and LiFePO<sub>4</sub> are the same. At each time

step, it was necessary to solve for  $c(\vec{x})$ ,  $u_i(\vec{x})$ ,  $u_j(\vec{x})$ ,  $\Delta\phi$ ,  $\bar{\varepsilon}_{11}$ ,  $\bar{\varepsilon}_{22}$ ,  $\bar{\varepsilon}_{33}$ , and  $\bar{\varepsilon}_{12}$ . The Matlab function ode15s was used for time integration, and the integral constraint was implemented with a singular mass matrix. Error tolerances of RelTol =  $10^{-3}$  and AbsTol =  $10^{-5}$  were used. A grid spacing of up to  $h = 2$  nm was sufficient to resolve the diffuse interface. A 100 × 100 grid was used for the discharging and size dependence simulations, and a 300 × 300 grid was used to simulate microstructure in larger particles. Simulations were run on a dual quad-core Linux workstation, used a maximum CPU usage of 400%, required

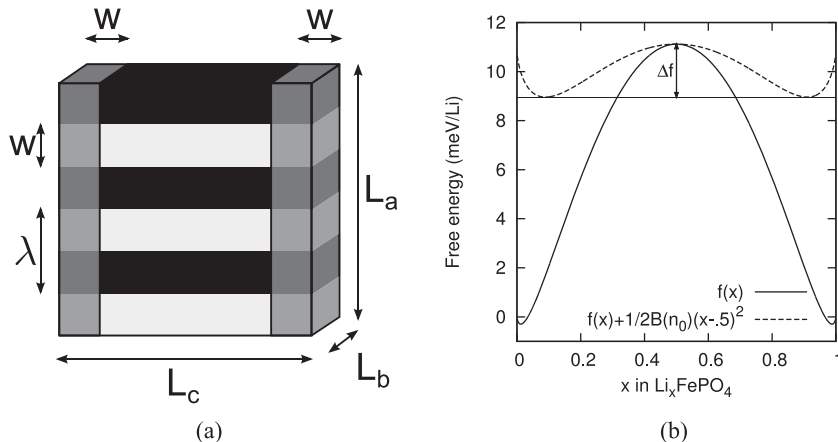


**Figure 7.** (a) Illustration of the stripe morphology in  $\text{Li}_5\text{FePO}_4$ . Elastic relaxation occurs in the shaded regions at the {001} surfaces of the particle. (b) Influence of coherent phase separation on free energy.

up to 4.4 Gb of memory, and took between a few minutes and a few hours to complete depending on the simulation.

**Phase-Field Parameters.** The inputs to the phase-field model that must be selected for the  $\text{Li}_x\text{FePO}_4$  system are the homogeneous free energy per particle  $f(c)$ , the gradient energy coefficient  $\kappa$ , the elastic stiffness  $C_{ijkl}$ , and the lattice mismatch  $\epsilon_{ij}^0$ . We use GGA+U first-principles calculations of  $C_{ijkl}$  for  $\text{FePO}_4$ <sup>4</sup> and lattice mismatch measured in ref 10. For  $f(c)$ , we assume a regular solution:

$$f(c) = \Omega c(1 - c) + kT(c \ln(c) + (1 - c)\ln(1 - c)) \quad (12)$$

The regular solution parameter  $\Omega$  and the gradient energy  $\kappa$  were obtained with a least-squares regression of the phase-field model to experimental measurements of the miscibility gap,<sup>9,28</sup> illustrated in Figure 4. Phase-field simulations were performed by allowing a square particle at  $x = 0.5$  to relax to equilibrium at zero current. The solubility limits were then found by taking the minimum and maximum compositions in the equilibrated microstructure.

The best fit was achieved with  $\Omega = 115 \text{ meV/Li}$  (11.1 kJ/mol) and  $\kappa = 3.13 \times 10^9 \text{ eV/m}$  ( $5.02 \times 10^{-10} \text{ J/m}$ ). The root-mean-square error was 2.3%. Both values are close to those used by Tang *et al.*<sup>16,42</sup> Sample C in Figure 4b had no measured strain and large particles that do not exhibit a size effect. Thus it is influenced by  $f(c)$  only. The fact that a particularly good fit is achieved with sample C supports the use of a regular solution for  $\text{Li}_5\text{FePO}_4$ .

**Stripe Scaling.** We adapt the arguments of Khachaturyan<sup>37,45</sup> to derive an expression for the period of striping in finite size  $\text{Li}_5\text{FePO}_4$  particles. Illustrated in Figure 7a, the stripes form to balance elastic relaxation at the {001} surfaces of the particle (energy/volume) and total interfacial energy (energy/area). The change in energy due to elastic relaxation,  $\Delta f = 4.77 \text{ MJ/m}^2$ , is illustrated in Figure 7b and is found with a common tangent construction applied to  $f(c) + 1/2B(\bar{n}_0)(c - X)^2$ , as described in refs 19, 20, and 46. Assuming that the width of relaxation  $w$  at the boundary is comparable to the size of the stripes, the change in energy due to relaxation and creation of phase boundaries is

$$\Delta E = 2\Delta f L_a L_b w + \frac{\gamma}{w} L_a L_b L_c \quad (13)$$

The equilibrium stripe size will minimize  $\Delta E$ , and so we solve for  $w$  when  $d\Delta E/dw = 0$ :

$$\frac{d\Delta E}{dw} = 2\Delta f L_a L_b - \frac{\gamma L_a L_b L_c}{w^2} = 0 \quad (14)$$

Solving for the stripe period  $\lambda = 2w$ , we obtain

$$\lambda = 2w = \sqrt{\frac{2\gamma L_c}{\Delta f}} \quad (15)$$

The  $\sqrt{L_c}$  dependence reveals that striping is an effect of finite size domains. As the domain size approaches infinity, the equilibrium state approaches two infinite domains separated by one interface.

**Conflict of Interest:** The authors declare no competing financial interest.

**Acknowledgment.** We are grateful to J. White for insightful discussions on numerical methods. This work was supported by the National Science Foundation under Contracts DMS-0842504 and DMS-0948071 and by a seed grant from the MIT Energy Initiative.

**Supporting Information Available:** Movies of the simulations in Figures 3 and 6 are provided in the Supporting Information. This material is available free of charge via the Internet at <http://pubs.acs.org>.

## REFERENCES AND NOTES

- Tang, M.; Carter, W. C.; Chiang, Y.-M. Electrochemically Driven Phase Transitions in Insertion Electrodes for Lithium-Ion Batteries: Examples in Lithium Metal Phosphate Olivines. *Annu. Rev. Mater. Res.* **2010**, *40*, 501–529.
- Morgan, D.; Van der Ven, A.; Ceder, G. Li Conductivity in  $\text{Li}_x\text{FePO}_4$  ( $M = \text{Mn, Fe, Co, Ni}$ ) Olivine Materials. *Electrochim. Solid-State Lett.* **2004**, *7*, A30–A32.
- Islam, M. S.; Driscoll, D. J.; Fisher, C. A. J.; Slater, P. R. Atomic-Scale Investigation of Defects, Dopants, and Lithium Transport in the  $\text{LiFePO}_4$  Olivine-Type Battery Material. *Chem. Mater.* **2005**, *17*, 5085–5092.
- Maxisch, T.; Ceder, G. Elastic Properties of Olivine  $\text{Li}_x\text{FePO}_4$  from First Principles. *Phys. Rev. B* **2006**, *73*, 174112.
- Padhi, A. K.; Nanjundaswamy, K. S.; Goodenough, J. B. Phospho-Olivines as Positive-Electrode Materials for Rechargeable Lithium Batteries. *J. Electrochem. Soc.* **1997**, *144*, 1188–1194.
- Delacourt, C.; Poizot, P.; Tarascon, J.-M.; Masquelier, C. The Existence of a Temperature-Driven Solid Solution in  $\text{Li}_x\text{FePO}_4$  for  $0 \leq x \leq 1$ . *Nat. Mater.* **2005**, *4*, 254–260.
- Dodd, J. L.; Yazami, R.; Fultz, B. Phase Diagram of  $\text{Li}_x\text{FePO}_4$ . *Electrochim. Solid-State Lett.* **2006**, *9*, A151–A155.
- Yamada, A.; Koizumi, H.; Nishimura, S.-i.; Sonoyama, N.; Kanno, R.; Yonemura, M.; Nakamura, T.; Kobayashi, Y. Room-Temperature Miscibility Gap in  $\text{Li}_x\text{FePO}_4$ . *Nat. Mater.* **2006**, *5*, 357–360.
- Meethong, N.; Huang, H.-Y. S.; Carter, W. C.; Chiang, Y.-M. Size-Dependent Lithium Miscibility Gap in Nanoscale  $\text{Li}_{1-x}\text{FePO}_4$ . *Electrochim. Solid-State Lett.* **2007**, *10*, A134–A138.
- Chen, G.; Song, X.; Richardson, T. J. Electron Microscopy Study of the  $\text{LiFePO}_4$  to  $\text{FePO}_4$  Phase Transition. *Electrochim. Solid-State Lett.* **2006**, *9*, A295–A298.
- Laffont, L.; Delacourt, C.; Gibot, P.; Wu, M. Y.; Kooyman, P.; Masquelier, C.; Tarascon, J. M. Study of the  $\text{LiFePO}_4/\text{FePO}_4$  Two-Phase System by High-Resolution Electron Energy Loss Spectroscopy. *Chem. Mater.* **2006**, *18*, 5520–5529.

12. Ramana, C. V.; Mauger, A.; Gendron, F.; Julien, C. M.; Zaghib, K. Study of the Li-Insertion/Extraction Process in LiFePO<sub>4</sub>/FePO<sub>4</sub>. *J. Power Sources* **2009**, *187*, 555–564.
13. Srinivasan, V.; Newman, J. Discharge Model for the Lithium Iron-Phosphate Electrode. *J. Electrochem. Soc.* **2004**, *151*, A1517–A1529.
14. Chung, S. Y.; Bloking, J. T.; Chiang, Y. M. Electronically Conductive Phospho-Olivines as Lithium Storage Electrodes. *Nat. Mater.* **2002**, *1*, 123–128.
15. Kang, B.; Ceder, G. Battery Materials for Ultrafast Charging and Discharging. *Nature* **2009**, *458*, 190–193.
16. Kao, Y.-H.; Tang, M.; Meethong, N.; Bai, J.; Carter, W. C.; Chiang, Y.-M. Overpotential-Dependent Phase Transformation Pathways in Lithium Iron Phosphate Battery Electrodes. *Chem. Mater.* **2010**, *22*, 5845–5855.
17. Bai, P.; Cogswell, D. A.; Bazant, M. Z. Suppression of Phase Separation in LiFePO<sub>4</sub> Nanoparticles during Battery Discharge. *Nano Lett.* **2011**, *11*, 4890–4896.
18. Malik, R.; Zhou, F.; Ceder, G. Kinetics of Non-equilibrium Lithium Incorporation in LiFePO<sub>4</sub>. *Nat. Mater.* **2011**, *10*, 587–590.
19. Cahn, J. W. On Spinodal Decomposition. *Acta. Metall.* **1961**, *9*, 795–801.
20. Cahn, J. W. On Spinodal Decomposition in Cubic Crystals. *Acta. Metall.* **1962**, *10*, 179–183.
21. Delmas, C.; Maccario, M.; Croguennec, L.; Le Cras, F.; Weill, F. Lithium Deintercalation in LiFePO<sub>4</sub> Nanoparticles via a Domino-Cascade Model. *Nat. Mater.* **2008**, *7*, 665–671.
22. Leriche, J. B.; Hamelet, S.; Shu, J.; Morcrette, M.; Masquelier, C.; Ouvrard, G.; Zerrouki, M.; Soudan, P.; Belin, S.; Elkaïm, E.; Baudelet, F. An Electrochemical Cell for Operando Study of Lithium Batteries Using Synchrotron Radiation. *J. Electrochem. Soc.* **2010**, *157*, A606–A610.
23. Meethong, N.; Huang, H.-Y.; Speakman, S.; Carter, W.; Chiang, Y.-M. Strain Accommodation during Phase Transformations in Olivine-Based Cathodes as a Materials Selection Criterion for High-Power Rechargeable Batteries. *Adv. Funct. Mater.* **2007**, *17*, 1115–1123.
24. Van der Ven, A.; Garikipati, K.; Kim, S.; Wagemaker, M. The Role of Coherency Strains on Phase Stability in Li<sub>x</sub>FePO<sub>4</sub>: Needle Crystallites Minimize Coherency Strain and Overpotential. *J. Electrochem. Soc.* **2009**, *156*, A949–A957.
25. Yamada, A.; Koizumi, H.; Sonoyama, N.; Kanno, R. Phase Change in Li<sub>x</sub>FePO<sub>4</sub>. *Electrochem. Solid-State Lett.* **2005**, *8*, A409–A413.
26. Kobayashi, G.; Nishimura, S.-i.; Park, M.-S.; Kanno, R.; Yashima, M.; Ida, T.; Yamada, A. Isolation of Solid Solution Phases in Size-Controlled LixFePO<sub>4</sub> at Room Temperature. *Adv. Funct. Mater.* **2009**, *19*, 395–403.
27. Badi, S.-P.; Wagemaker, M.; Ellis, B. L.; Singh, D. P.; Borghols, W. J. H.; Kan, W. H.; Ryan, D. H.; Mulder, F. M.; Nazar, L. F. Direct Synthesis of Nanocrystalline Li<sub>0.90</sub>FePO<sub>4</sub>: Observation of Phase Segregation of Anti-site Defects on Delithiation. *J. Mater. Chem.* **2011**, *21*, 10085–10093.
28. Wagemaker, M.; Singh, D. P.; Borghols, W. J.; Lafont, U.; Haverkate, L.; Peterson, V. K.; Mulder, F. M. Dynamic Solubility Limits in Nanosized Olivine LiFePO<sub>4</sub>. *J. Am. Chem. Soc.* **2011**, *133*, 10222–10228.
29. Dreyer, W.; Jamnik, J.; Gühlke, C.; Huth, R.; Moskon, J.; Gaberscek, M. The Thermodynamic Origin of Hysteresis in Insertion Batteries. *Nat. Mater.* **2010**, *9*, 448–453.
30. Dreyer, D.; Gühlke, C.; Huth, R. The Behavior of a Many-Particle Electrode in a Lithium-Ion Battery. *Physica D* **2011**, *240*, 1008–1019.
31. Singh, G. K.; Ceder, G.; Bazant, M. Z. Intercalation Dynamics in Rechargeable Battery Materials: General Theory and Phase-Transformation Waves in LiFePO<sub>4</sub>. *Electrochim. Acta* **2008**, *53*, 7599–7613.
32. Burch, D.; Singh, G.; Ceder, G.; Bazant, M. Z. Phase-Transformation Wave Dynamics in LiFePO<sub>4</sub>. *Solid State Phenom.* **2008**, *139*, 95–100.
33. Cahn, J. W.; Hilliard, J. E. Free Energy of a Nonuniform System. I. Interfacial Free Energy. *J. Chem. Phys.* **1958**, *28*, 258–267.
34. van der Waals, J. D. The Thermodynamic Theory of Capillarity under the Hypothesis of a Continuous Variation of Density. *Verhandel. Konink. Akad. Weten. Amsterdam (Sect. 1)* **1893**, *1*, 8. Translation by Rowlinson, J. S. *J. Stat. Phys.* **1979**, *20*, 197–244.
35. Wang, Y. U.; Jin, Y. M. M.; Khachaturyan, A. G. Phase Field Microelasticity Theory and Simulation of Multiple Voids and Cracks in Single Crystals and Polycrystals under Applied Stress. *J. Appl. Phys.* **2002**, *91*, 6435–6451.
36. Garcia, R. E.; Bishop, C. M.; Carter, W. C. Thermodynamically Consistent Variational Principles with Applications to Electrically and Magnetically Active Systems. *Acta Mater.* **2004**, *52*, 11–21.
37. Khachaturyan, A. G. *Theory of Structural Transformations in Solids*; Dover Publications: New York, 2008; pp 198–230 and 315–334.
38. Bazant, M. Z. 10.626 Electrochemical Energy Systems; Massachusetts Institute of Technology: MIT OpenCourseWare, <http://ocw.mit.edu>, License: Creative Commons BY-NC-SA, 2011.
39. Burch, D.; Bazant, M. Z. Size-Dependent Spinodal and Miscibility Gaps for Intercalation in Nanoparticles. *Nano Lett.* **2009**, *9*, 3795–3800.
40. Malik, R.; Burch, D.; Bazant, M.; Ceder, G. Particle Size Dependence of the Ionic Diffusivity. *Nano Lett.* **2010**, *10*, 4123–4127.
41. Lee, J.; Zhou, W.; Idrobo, J. C.; Pennycook, S. J.; Pantelides, S. T. Vacancy-Driven Anisotropic Defect Distribution in the Battery-Cathode Material LiFePO<sub>4</sub>. *Phys. Rev. Lett.* **2011**, *107*, 085507.
42. Tang, M.; Belak, J. F.; Dorr, M. R. Anisotropic Phase Boundary Morphology in Nanoscale Olivine Electrode Particles. *J. Phys. Chem. C* **2011**, *115*, 4922–4926.
43. Khachaturyan, A. Some Questions Concerning the Theory of Phase Transformations in Solids. *Sov. Phys. Solid State* **1967**, *8*, 2163–2168.
44. Stanton, L. G.; Bazant, M. Z. Phase Separation with Anisotropic Coherency Strain. **2012**, arXiv:1202.1626v1.
45. Khachaturyan, A. G. Elastic Strains during Decomposition of Homogeneous Solid Solutions: Periodic Distribution of Decomposition Products. *Phys. Status Solidi B* **1969**, *35*, 119–132.
46. Cahn, J. W. Coherent Fluctuations and Nucleation in Isotropic Solids. *Acta. Metall.* **1962**, *10*, 907–913.
47. Porter, D. A.; Easterling, K. E.; Sherif, M. Y. *Phase Transformations in Metals and Alloys*; CRC Press: Boca Raton, FL, 2009; pp 141–146 and 181–192.
48. Nauman, E. B.; Balsara, N. P. Phase Equilibria and the Landau-Ginzburg Functional. *Fluid Phase Equilib.* **1989**, *45*, 229–250.
49. Andersson, A. S.; Thomas, J. O.; Kalska, B.; Haggstrom, L. Thermal Stability of LiFePO<sub>4</sub>-Based Cathodes. *Electrochem. Solid-State Lett.* **2000**, *3*, 66–68.
50. Mestre-Aizpurua, F.; Hamelet, S.; Masquelier, C.; Palacin, M. R. High Temperature Electrochemical Performance of Nanosized LiFePO<sub>4</sub>. *J. Power Sources* **2010**, *195*, 6897–6901.
51. Munoz-Rojas, D.; Leriche, J. B.; Delacourt, C.; Poizot, P.; Palacin, M. R.; Tarascon, J. M. Development and Implementation of a High Temperature Electrochemical Cell for Lithium Batteries. *Electrochem. Commun.* **2007**, *9*, 708–712.
52. Cahn, J. W.; Hilliard, J. E. Free Energy of a Nonuniform System. III. Nucleation in a Two-Component Incompressible Fluid. *J. Chem. Phys.* **1959**, *31*, 688–699.
53. Wang, L.; Zhou, F.; Meng, Y. S.; Ceder, G. First-Principles Study of Surface Properties of LiFePO<sub>4</sub>: Surface Energy, Structure, Wulff Shape, and Surface Redox Potential. *Phys. Rev. B* **2007**, *76*, 165435.